ADVANCED OPTICAL MATERIALS
www.advopticalmat.de

Photonic Integrated Circuit for Rapidly Tunable Orbital Angular Momentum Generation Using Sb_2Se_3 Ultra-Low-Loss Phase Change Material

*Md Shah Alam, Rudra Gnawali, Joshua R. Hendrickson, Diane Beamer, Tamara E. Payne, Andrew Volk, and Imad Agha**

The generation of rapidly tunable optical vortex (OV) beams is one of the most demanding research areas of the present era as they possess orbital angular momentum (OAM) with additional degrees of freedom that can be exploited to enhance signal-carrying capacity by using mode division multiplexing and information encoding in optical communication. Particularly, rapidly tunable OAM devices at a fixed wavelength in the telecom band stir extensive interest among researchers for both classical and quantum applications. This article demonstrates the realistic design of a Si-integrated photonic device for rapidly tunable OAM wave generation at a 1550-nm wavelength by using an ultra-low-loss phase change material (PCM) embedded with a Si-ring resonator with angular gratings. Different OAM modes are achieved by tuning the effective refractive index using rapid electrical switching of Sb_2Se_3 film from amorphous to crystalline states and vice versa. The generation of OAM waves relies on a traveling wave modulation of the refractive index of the micro-ring, which breaks the degeneracy of oppositely oriented whispering gallery modes. The proposed device is capable of producing rapidly tunable OV beams, carrying different OAM modes by using electrically controllable switching of ultra-low-loss PCM Sb_2Se_3.

1. Introduction

Orbital angular momentum (OAM)[1] is an additional degree of freedom of a photon, in addition to polarization and spin, which can be exploited in numerous applications such as optical communications,[2,3] quantum optics,[4] optical trapping,[5] and lithography.[6] Since the development of OAM properties of light beams, researchers have aimed to investigate various techniques for tuning between different modes. As different OAM modes are used as bits in both quantum and classical OAM optical communications, the switching between OAM modes could dramatically enhance the data rate[7] by expanding the encoding basis.

Circularly polarized light contains spin angular momentum (SAM) of $\sigma\hbar$ ($\sigma = \pm 1$) per photon. However, in 1992, Allen et al. demonstrated that the optical vortex (OV) light also possesses OAM[8] which is expressed in $l\hbar$ ($l = \pm 1, \pm 2, \pm 3, \ldots$) per photon. This provides a theoretically infinite number of channels that can be multiplexed with existing beam states since l can take any value.[1–7,9–11] These states can be added to the existing beam states that use wavelength, amplitude, phase, time, and polarization of light to encode information. For the OV, the value of the phase's integral of the electric field around a path enclosing the vortex is equal to $l\hbar$, where l is the topological charge and $\hbar$ is Planck's constant divided by 2π. This OAM constitutes an additional degree of freedom[3,12] as the quantum characteristics $l\hbar$ do not interfere with each other.

The generation of OAM beams requires manipulation of the polarization and spatial mode of laser light. There are several methods to generate OAM beams which involve q-plates and phase retarders,[13] nematic spatial light modulators,[14] spatially varying retarders,[15] catenary optics,[16] interferometric methods,[17] and integrated photonics such as Si-ring resonators with azimuthally varying grating elements[7] as well as STAR shaped outcouplers.[18] Among these methods, integrated photonics could potentially provide more flexibility for tuning different modes at high speeds. As an example, for Si-ring resonators with azimuthally varying grating elements, a single whispering gallery mode (WGM) is excited by a unidirectional wave from the bus waveguide, either clockwise or counterclockwise,

M. S. Alam, I. Agha
Department of Electro-Optics and Photonics
University of Dayton
Dayton, OH 45469, USA
E-mail: iagha1@udayton.edu
R. Gnawali, D. Beamer, T. E. Payne, A. Volk
Applied Optimization, Inc
3040 Presidential Dr. Suite 100, Fairborn, OH 45324, USA
J. R. Hendrickson
Air Force Research Laboratory
Sensors Directorate
Wright-Patterson Air Force Base
Fairborn, OH 45433, USA
I. Agha
Department of Physics
University of Dayton
Dayton, OH 45469, USA
The ORCID identification number(s) for the author(s) of this article can be found under https://doi.org/10.1002/adom.202200098.

DOI: 10.1002/adom.202200098

and the resonators emit the OAM radiation vertically. Other integrated optics approaches for generating OAM radiation include an Archimedean spiral-shaped waveguide,[19–21] a collection of subwavelength cavities designed for broadband OAM vertical radiation,[22] and phased array nanoantennas.[23]

Since the unique advantage of using optical OAM relies on properly accessing multiple OAM states, it is therefore desirable to implement devices that generate rapidly tunable OAM states of light, especially in an integrated form to afford large scale-up and low-cost. There are several prior demonstrations that have produced different OAM states on-chip by coupling to different ports on a passive chip,[24] adjusting the operating wavelength,[7] or by introducing heaters into Si as a mechanism for tuning.[9,25] However, while such devices have shown the principle of tunability, fast tuning of OAM modes would benefit from better mechanisms for tuning than was previously explored.

In this paper, a realistic and highly realizable model of a compact, integrated silicon photonic circuit with µs level switching time composed of a Si-ring resonator with angular grating elements, embedded with ultra-low-loss Sb_2Se_3 phase change material (PCM)[26] is presented to generate continuously and rapidly tunable OAM states. The switching speed is comparable to or even exceeds that of existing literature.[27–29] The compactness and flexibility of the device hold enormous promise for integration with other silicon photonic components for a wide range of applications.

2. Integrated Photonics for Cylindrical Vector Vortices

Figure 1a represents the schematic of the OAM transceiver. This integrated photonic device has three basic elements: an access waveguide, circular resonator, and angular gratings on the inner wall of the circular resonator. When the access waveguide is excited by a laser beam, the light is coupled into the ring resonator. At resonance conditions, WGMs are produced and the angular grating elements emit a vortex beam carrying OAM traveling normal to the ring resonator plane.[7] The emitted vortex beam is also referred to as cylindrical vector vortices (CVVs) as it exhibits cylindrically symmetric intensity distribution and polarization.[30,31] The resonance mode of the emitted wave depends on the number of grating elements, radius, effective refractive index of the ring resonator, and wavelength. The gratings scatter the WGMs as well-controlled OAM states for free-space propagation in a similar fashion to waveguide grating couplers[32] scattering Gaussian modes, acting as an OV emitter. When the quasi-Transverse Electric (TE) mode of different laser wavelengths is coupled into the access waveguide, various cavity resonances are excited, and azimuthally polarized vector vortices with quantized OAM waves are emitted from the device. Conversely, when an azimuthally polarized vortex beam of different OAM states is applied toward the ring resonator containing the grating elements, then at the resonance conditions, the WGMs are confined into the ring resonator and back-coupled into the access waveguide so that the device acts as an OAM detector.[32]

The Jones vector of the output CVVs carrying OAM can be represented by:[33,34]

$$\mathbf{E}_{\text{out}} \propto \frac{1}{2}\left\{\sqrt{1+\sigma}e^{i(l_{\text{TC}}+1)\varphi}\begin{bmatrix}1\\ i\end{bmatrix}+\sqrt{1-\sigma}e^{i(l_{\text{TC}}-1)\varphi}\begin{bmatrix}1\\ -i\end{bmatrix}\right\} \quad (1)$$

where $l_{\text{TC}} = p - q$ is the Topological Charge (TC),[7] and σ ($|\sigma| \leq 1$) is the transverse spin state in the near field evanescent wave at the sidewalls of the ring resonator due to grating perturbation. For the transverse SAM, left (right) handed spin is defined as $\sigma > 0$ (< 0). q and p are the numbers of the grating elements around the circular resonator and the WGM azimuthal mode order (numbers of the optical periods in WGMs), respectively. The number of the optical periods is defined as:

$$p = \frac{2\pi R n_{\text{eff}}}{\lambda} \quad (2)$$

where n_{eff} and R are the effective index of the WGMs and the inner radius of the circular resonator, respectively, and λ is the wavelength of illumination which is around 1550 nm for the proposed design.

The total angular momentum (TAM) of the emitted paraxial OV beam can be considered as the sum of the OAM and SAM components which are associated with the spatial properties and polarization of light respectively.[34] The angular phase

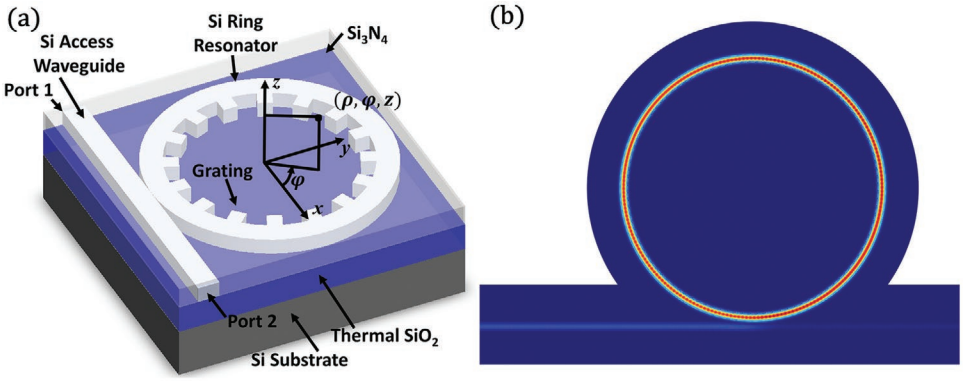

Figure 1. a) Schematic of the Si-ring resonator with angular grating elements for OAM generation. b) Electric field intensity inside the ring and access waveguide at resonance wavelength 1550.85 nm.

variation in the transverse component of CVVs is a linear function of the cylindrical coordinate φ and can be written as:[34]

$$\Phi_{\mathrm{p}} = (l_{\mathrm{TC}}\varphi \pm \sigma\varphi) \tag{3}$$

where $l_{\mathrm{TC}}\varphi = (p - q)\varphi$ arises from the first order diffraction of the grating elements (OAM) and $\pm\ \sigma\varphi$ corresponds to the local transverse spin state (SAM) while counter-clockwise CCW (+) or clockwise CW (–) WGMs travel around the ring resonator. When the polarization at the grating scatterer location reaches one of the circular polarizations (LHCP: $\sigma = +1$, RHCP: $\sigma = -1$) then the superposition reduces to $(l_{\mathrm{TC}} \pm 1)\varphi$. On the other hand, the z component (along the CVVs propagation direction) of the SAM and OAM carried by the CVVs can be represented by:[34]

$$S_z = \sigma\hbar, \qquad L_z = (l_{\mathrm{TC}} - \sigma)\hbar \tag{4}$$

where $\hbar$ is the reduced Planck constant. Here, the TAM of the z component,

$$J_z = S_z + L_z = l_{\mathrm{TC}}\hbar = (p - q)\hbar \tag{5}$$

is conserved with the azimuthal mode order p of WGM and the number of grating elements q regardless of the transverse spin state (SAM). This is due to the rotationally symmetric anisotropy orientation of the scatterer grating elements.

Here, an integrated OAM generator/transceiver is designed using a Si ring resonator which is built on top of a standard 220-nm-thick Si-on-Insulator (SOI) wafer. This is chosen for compatibility with foundry processing in the future. The width of the access waveguide and ring resonator is 550 nm, and the inner radius of the ring resonator is 9.45 µm. The length and width of the grating elements are kept at 15% of the grating period (Λ) (81.7 nm). The coupling gap between the access waveguide and the circular resonator is kept at 120 nm. The number of grating elements is chosen to be 104 to achieve an OAM wave with a topological charge ($l_{TC} = p - q$) = 0 within the range of 1540 to 1550 nm. The Si waveguide and the ring resonator with grating elements are on top of a 2-µm thermal oxide (SiO_2) and buried in 1.5 µm of LPCVD (low pressure chemical vapor deposition)/PECVD (plasma enhanced chemical vapor deposition) Si_3N_4. The topological charge ($l_{\mathrm{TC}} = p - q$) can take any integer value depending on the difference of p and q. According to Equation (2), p increases with the increase of the effective refractive index of the ring resonator but decreases with the increase of the wavelength of the excited beam for a fixed radius ring resonator. A 3D finite element method model (COMSOL Multiphysics) is used to perform numerical simulation to find the resonance wavelengths for different OAM modes. Port 1 (Figure 1a) is excited with TE 01 mode and wavelengths are tuned from 1510 to 1585 nm. Figure 1b shows the electric field intensity inside the ring resonator while it is at resonance and emits CVV carrying OAM wave with $l = -1$. **Figure 2** represents the intensity and the corresponding phase of the different emitted OAM waves radiated normal to the ring resonator plane toward (+ z) direction at different resonant wavelengths. According to Equation (5), the z component of radiated CVVs represents TAM which equals the topological charge of the OAM wave (l_{TC}). Figure 2a,b represents the $|E_z|^2$ and the phase of the z component of the radiated wave respectively. According to Figure 2b, the proposed ring resonator radiates OAM waves with $l_{\mathrm{TC}} = +3, +2, +1, 0, -1, -2, -3, -4$ at 1511.60, 1521.20, 1531.00, 1540.50, 1550.85, 1561.25, 1571.55, and 1581.90 respectively. The corresponding radiation efficiencies are found to be 25.7%, 25.4%, 29.8%, 26.6%, 28.5%, 26.1%, 29.2% and 29.5% respectively. The TAM $l_{TC} \pm 1$ (due to OAM and SAM in the transverse components (I_x, I_y)) depends the transverse spin σ (+/-) and rotation of the WGMs (CCW/CW) in the ring resonator as can be observed in Figure 2c (I), Figure 2d (phase of E_y, φ_y), Figure 2e (phase of E_x, φ_x). Figure 2f represents the phase difference of E_y and E_x, $\varphi_y - \varphi_y = \mp\pi/2$ which demonstrates the existence of SAM in CVVs along with the OAM. From Figure 2d–f, it is observed that the radiated CVVs possess RHCP for $l_{\mathrm{TC}} > 0$, while LHCP for $l_{\mathrm{TC}} < 0$ along with the OAM. The Free Spectral Range (FSR) is found to be close to 10 nm. Increasing the radius of the ring resonator reduces the value of the FSR and increases the number of modes in a given spectral range.

3. Rapidly Tunable OAM Generator and Transceiver

For a specific design, the number of grating elements is fixed. Therefore, tuning different OAM modes at a specific wavelength requires the change of the effective refractive index of the ring resonator hence changing the WGM order. Similarly, a large refractive index change is required to tune different modes for a larger FSR. At the expense of increasing the Si-ring size, the adjacent mode can be brought closer. However, to make the device more compact, we have considered a 9.45-µm ring in which the adjacent modes are separated by ≈10 nm.

Traditionally, PCMs allow for tuning of the refractive index due to the inherent dielectric constant contrast as the material transitions from a glassy to a crystalline state in response to a thermal stimulus.[26,35–37] As such, the effective refractive index of the ring resonator can be tuned by introducing a PCM film with a larger refractive index contrast between the amorphous and crystalline states. The PCM film can be closely placed on top of the ring resonator in the cladding region as shown in the schematic diagram of **Figure 3**a. By recurrently switching the phase of the PCM, the effective refractive index can be rapidly varied to tune different OAM modes. There are several types of PCMs that can provide a significant amount of refractive index change while changing the phase from amorphous to crystalline states and vice versa. However, most of them are very lossy at the telecom band. For example, a complex refractive indices for amorphous and crystalline states are $4.2402 + i\ 0.05094$ and $6.1095 + i\ 0.72127$, respectively, for GST[38] and $4.2 + i\ 0.034$ and $5.5 + i0.27$, respectively, for GeTe.[39] Therefore, they are not suitable for designing a tunable OAM device as any high-Q resonance will be washed out. However, Sb_2Se_3 and Sb_2S_3 are promising ultra-low-loss PCMs at 1550 nm.[26] The amorphous and crystalline refractive indices of Sb_2Se_3 are $3.285 + i0$, $4.05 + i0$ ($\Delta n = 0.765 + i0$) respectively and for the Sb_2S are $2.712 + i0$, $3.308 + i0$ ($\Delta n = 0.596 + i0$) respectively. Although they have a comparatively low refractive index contrast, but a thin film of

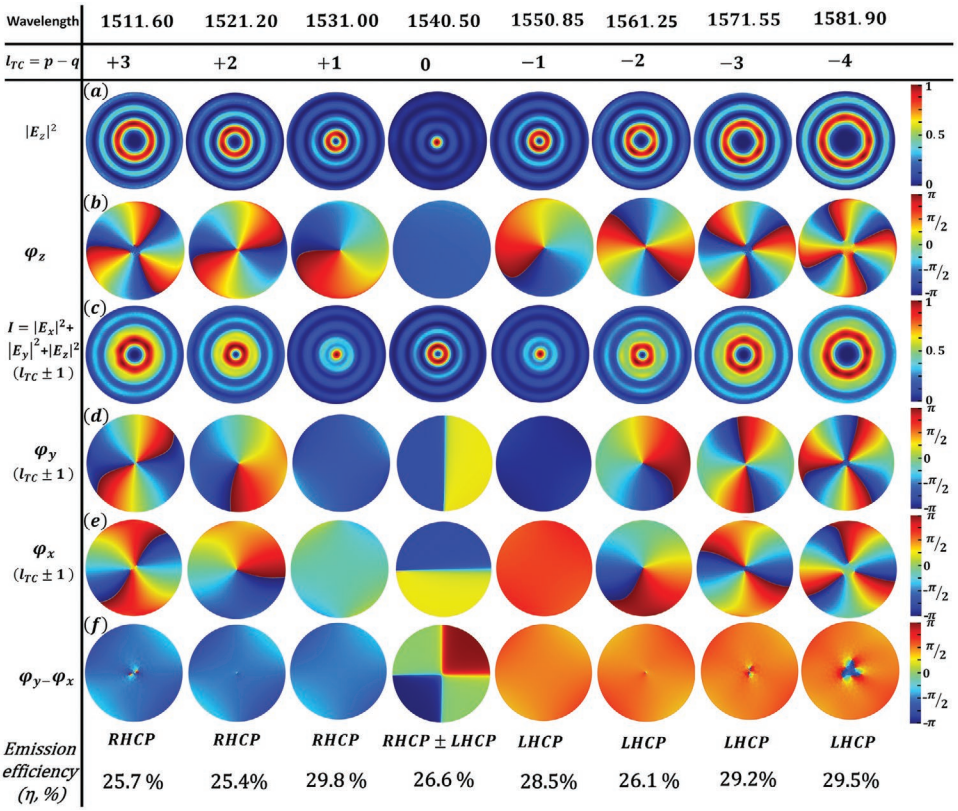

Figure 2. Generation of different OAM modes from Si ring resonator with grating elements by tuning wavelengths from 1510 to 1585 nm. Ring radius is 9.45 µm. Different OAM modes of l = +3, + 2, +1, 0, −1, −2, −3, − 4 are generated at 1511.60, 1521.2, 1531.00, 1540.50, 1550.85, 1561.25, 1571.55, 1581.90 respectively. a) Longitudinal component of electric field intensity ($|E_z|^2$) of different OAM modes l = +3, + 2, +1, 0, −1, −2, −3, − 4. b) Spiral phase of longitudinal component of electric field E_z of different OAM modes. c) Total electric field intensity of emitted CVVs containing total angular momentum (TAM) of $l_{TC} \pm 1$. d) Phase of transverse E_x component of the emitted vortex beam (with topological charge $l_{TC} \pm 1$). e) Phase of transverse E_y component. f) Phase difference between transverse E_y and E_x ($E_x(\mp\pi/2)$) showing the presence of spin angular momentum (SAM) in the emitted vortex beam along with the OAM.

Sb_2Se_3/Sb_2S_3 can be placed very close to the Si-ring resonator as they are lossless. Therefore, by switching the film between its two phases, a reasonable amount of effective refractive index change is incurred and thereby different OAM modes can be tuned. This can be attributed to the Figure of merit that defines optical PCMs: mainly the contrast of refractive index versus the increase in extinction coefficient.

For the initial design, a 9.45 µm (inner radius) ring resonator with 110 grating elements and a 105-nm-thin Sb_2Se_3 (PCM) film ring on top of the Si ring separated by 50 nm thin Si_3N_4 film is chosen to enable tuning between different OAM modes at 1550 nm wavelength. The width and the thickness of the ring resonator are considered to be 550 and 220 nm respectively which are the same as the above designed OAM generator at different wavelengths. The phase of the PCM film ring is considered to be thermally partially switched by 120 nm thin indium tin oxide (ITO) film ring heater. The inner/outer radius, and width of the PCM and ITO rings are considered to be the same as the Si ring resonator. The ITO film is selected as it can be prepared as of optically very low loss[40] and moderately thermally conductive. Figure 3a,b shows the schematics of the tunable OAM generation by partial phase change. The FEM analysis is conducted to achieve different OAM modes at 1550 nm by considering different levels of partial switching of the PCM. Figure 3c–g represents the generation of different OAM modes and their corresponding emission efficiencies by partially changing the phase of the Sb_2Se_3 film. For the simplicity of the analysis, the overall refractive index of the Sb_2Se_3 film is considered to be between 3.285 (fully amorphous) and 4.05 (fully crystallized) as an effect of partial crystallization. The validity of the "overall refractive index of the PCM film" approach is supported by comparing the result of this approach with a "different amorphous and crystalline layer inside the PCM film" approach in Figure 3g. The effect of variation of the different parameters of the proposed tunable OAM device on the OAM radiation efficiency such as the coupling gap between the access waveguide and the Si ring resonator, the width and extrusion length of the grating elements, and the presence or absence of the grating on the PCM and the ITO film ring layers are analyzed. Figure 3b represents the schematic of the initial proposed design of the tunable OAM device with the presence of multilayer gratings. Initially, the grating elements are considered to be on the Si ring resonator only and the coupling gap, width, and extrusion lengths are kept the same as the above designed OAM generators at different wavelengths, that is, 120 nm and 15% of the grating period

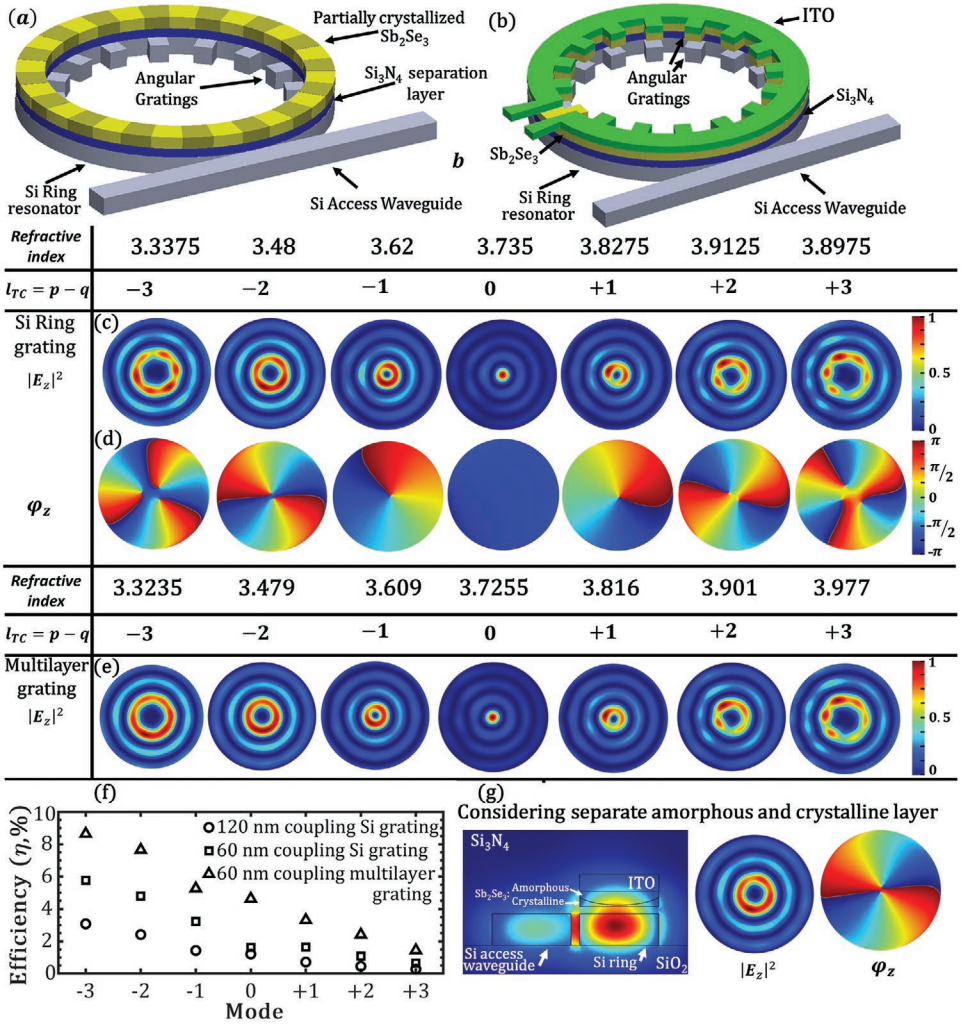

Figure 3. Generation of different modes of OAM waves at 1550 nm by embedding Sb_2Se_3 PCM: a,b) Schematic of tunable OAM generator consisting of Si waveguide, ring resonator with angular gratings, and105-nm-thick Sb_2Se_3 PCM placed on top of the ring with a separation of 50 nm. The Si waveguide is on top of a thermally evaporated SiO_2 layer and buried by a Si_3N_4 layer. a) Simple Schematic of tunable OAM generator. b) Simple Schematic of tunable OAM generator with multilayer grating elements. c) Longitudinal component of electric field intensity ($|E_z|^2$) of different OAM modes $l = -3$, -2, -1, 0, +1, +2, +3, coupling gap = 120 nm, width/length of grating element = 81.7 nm, grating elements on Si ring resonator only. d) Spiral phase of longitudinal component of electric field E_z of different OAM modes. e) Longitudinal component of electric field intensity ($|E_z|^2$) of different OAM modes $l = -3$, -2, -1, 0, +1, +2, +3, coupling gap = 60 nm, width of grating element = 81.7 nm, extrusion length of grating element = 100 nm, multilayer (Si, PCM, ITO) grating elements. f) Emission efficiency of OAM waves for different device parameters (coupling gap between access waveguide and ring resonator, grating element's extrusion length, and presence/absence of grating elements at the sidewall of PCM and ITO rings) conditions. Circles correspond to coupling gap of 120 nm, grating width/length = 81.7 nm, Si ring grating only; squares correspond to coupling gap of 60 nm, grating width = 81.7 nm, grating extrusion length = 100 nm, Si ring grating only; and triangles correspond to coupling gap of 60 nm, grating width = 81.7 nm, grating extrusion length = 100 nm, grating elements are present at all (Si, PCM and ITO ring) layers. g) Electric field distribution inside the access waveguide and rings, and generated $l = -2$ OAM wave for partially switched 105 nm PCM film. 90 nm thin layer is considered as amorphous (refractive index of 4.05) and 15 nm layer is considered as crystalized (refractive index of 3.28) with curvature interface between them. The corresponding generated wave is analogous to overall refractive index of 3.48 of PCM layer.

(81.7 nm) respectively. The simulation results of Figure 3c,d correspond to these design parameters. From Figure 3c,d, it is observed that $l_{TC} = -3$, $l_{TC} = -2$, $l_{TC} = -1$, $l_{TC} = 0$, $l_{TC} = +1$, $l_{TC} = +2$, $l_{TC} = +3$ can be achieved by partially changing the phase of the Sb_2Se_3 from amorphous to crystalline by considering overall refractive index as 3.3375, 3.48, 3.62, 3.735, 3.8275, 3.9125, and 3.9875 respectively. The corresponding emission efficiency are found to be 3.08%, 2.42%, 1.43%, 1.21% 0.71%, 0.45% and 0.28% respectively (Figure 3f). The lower emission efficiency is attributed to the leaking of the optical power from the Si ring resonator to the high refractive index (around 4 while crystalized) 105 nm Sb_2Se_3 film ring. Moreover, the presence of 120 nm lossy ITO film ring on top of the PCM film ring causes absorption while light circulates inside the rings. With the increase of the crystallization fraction more optical power leaks from Si ring resonator and confines to the chalcogenide layer. Therefore, the efficiency significantly decreases with the increase of the crystallization fraction. The efficiency can

be improved by engineering the coupling between the Si ring and the access waveguide to the critical coupling point.[41,42] Moreover, the width and extrusion length of the grating elements contribute to the emission efficiency to some extent. The grating elements' width of 15% of the grating period and extrusion length of 100 nm are found to be optimized dimensions to radiate OAM wave with the present condition. Hence, the radiation efficiency increases by around a factor of two or higher by using 100 nm grating length and reducing the coupling gap to 60 nm. The overall refractive index of PCM of 3.3325, 3.4875, 3.617, 3.7265, 3.8255 3.910, and 3.9865 correspond to $l_{TC} = -3$, $l_{TC} = -2$, $l_{TC} = -1$, $l_{TC} = 0$, $l_{TC} = +1$, $l_{TC} = +2$, $l_{TC} = +3$ respectively with radiation efficiency of 5.77%, 4.79%, 3.23%, 1.63%, 1.08% and 0.64% respectively. Furthermore, introducing the multilayer grating elements at the sidewalls of the PCM and ITO rings significantly improves the radiation efficiency. The 8.65%, 7.65% 5.26%, 4.63%, 3.31%2.41% and 2.45% radiation efficiencies are achieved for $l_{TC} = -3$, $l_{TC} = -2$, $l_{TC} = -1$, $l_{TC} = 0$, $l_{TC} = +1$, $l_{TC} = +2$, $l_{TC} = +3$ respectively at PCM's average (overall) refractive index of 3.3235, 3.479, 3.609, 3.7255,3.816, 3.901, and 3.977 respectively as shown in Figure 3e,f. Instead of considering the average refractive index of the PCM as fractional phase change, if the PCM film is considered to be two or more layers of amorphous and crystalline area, then similar types of results can be achieved. Figure 3g shows that $l_{TC} = -2$ OAM wave can be emitted from the device, if the 105 nm PCM is considered to be two different layers consisting 90 nm amorphous layer and 15 nm crystalline layer of curved interface. This result resembles that of the partially crystalize/amorphize 105 nm Sb_2Se_3 film with an average refractive index of around 3.48. Therefore, the proposed simplified approach of considering the average refractive index in between the amorphous and crystalline refractive index is good enough to represent the partial phase change and to estimate the emission efficiency of the different OAM modes.

4. Comparison of Different Design Options for Tunability

A PCM can be reversibly switched between phases either optically, electrically, or thermally- using micro/nano heater. For optical switching, the desired fraction of phase change can be achieved by controlling laser pulse duration and pulse power.[26] The advantage of optical switching is that it does not require any electrically conductive material (which is usually lossy) to be placed on top of the PCM, hence it can provide efficient OAM emission with a very simple design. Moreover, optical switching is inherently faster than the thermal switching which can provide rapidly tunable OAM waves. On the other hand, the electrical and thermal switching options provide more compact integrated photonic device option with the expense of comparatively lower efficient OAM generation due to the use of electrically conductive lossy material which adversely affects the emission efficiency. However, ITO is an optically transparent conductive material for which the imaginary part of the complex refractive index can be controlled and minimized by controlling the parameters of the film fabrication procedure.[40] Theretofore, it is still possible to generate a moderately efficient OAM wave with the presence of ITO. In this work, to achieve the desired fraction of phase change of the Sb_2Se_3 film, four different types of realistic designs using ITO-based nano-heater circuits are proposed as shown in **Figure 4**a–d. A rapid switching of Sb_2Se_3 film using joule heating of the ITO based nano-heater circuits can be achieved using the proposed design. The Sb_2Se_3 film needs to be cooled down from above its crystallization temperature (200 °C) to crystallize the amorphous Sb_2Se_3 film.[26] To achieve reamorphization, the temperature should be raised to the melting point (610 °C) and needs to be cooled down faster than the crystallization speed, leaving it in an amorphous state.

The feasibility of the reversible switching for the proposed designs to tune OAM modes from $l = -3$ to $l = +2$ at 1550 nm depends on the effective change of the refractive index of the ring resonator which can be evaluated by Equation (6):

$$l = p - q = \frac{2\pi R n_{\text{eff}}}{\lambda} - q \tag{6}$$

For our design, the number of grating elements is 110, the inner ring radius is $R = 9.45$ μm, and $\lambda = 1550$ nm. Therefore, the effective index of the ring resonator should be tuned to 2.7932, 2.8193, 2.8454, 2.8715, 2.8976, and 2.9237 to generate $l = -3$, −2, −1, 0, +1, +2, respectively. The phase of the appropriate fraction of cladding Sb_2Se_3 film needs to be changed by applying a pulse voltage of proper magnitude and pulse duration on the nano-heater to achieve the required effective refractive index to tune the OAM waves from $l = -3$ to $l = +2$.

Design 1: Figure 4a represents the schematic of an ITO nano-heater based OAM generator. A 220-nm-thick Si-ring resonator with a 9.45 μm inner radius and 110 azimuthal grating elements and a closely placed access waveguide can be used to generate OAM waves. The ring resonator and access waveguide are covered with a very thin layer of Si_3N_4. A Sb_2Se_3 PCM ring of the same radius as the Si ring is placed on top of the Si-ring resonator. Five different ITO nano-heaters are placed in between each grating element as shown schematically in Figure 4a. The nano-heaters are connected in a series with the corresponding nano-heaters of each grating element according to the connection shown in Figure 4a. Each ITO nano-heater is connected to a different ultra-short pulse voltage source. V_1, V_2, V_3, V_4, and V_5 are applied at Port 3, Port 4, Port 2, Port 5, and Port 1, respectively, corresponding to the first grating element. All five ports of the 110th grating element are connected to the electrical ground. Initially, the high fraction of the Sb_2Se_3 PCM is considered to be in an amorphous state and excites an OAM wave of $l = -3$. By applying a pulse voltage, V_1, at Port 3, a small fraction of the Sb_2Se_3 element is crystallized to excite an OAM wave of the $l = -2$ mode. Similarly, by applying V_1 and V_2, an $l = -1$ mode, by V_1, V_2 and V_3 an $l = 0$ mode, by V_1, V_2, V_3 and V_4 an $l = +1$ mode, and by V_1, V_2, V_3, V_4 and V_5 an $l = +2$ mode can be excited. The amorphization voltage, a comparatively higher voltage with a shorter pulse, is then applied to all of the ITO nano-heaters to reamorphize the necessary fraction of the Sb_2Se_3 ring to achieve an $l = -3$ mode. Initially, the required pulse voltage amplitude and pulse duration can be experimentally evaluated.

Design 2: Figure 4b represents a tunable OAM wave generator with multilayer Sb_2Se_3 PCM and ITO nano-heaters. In this

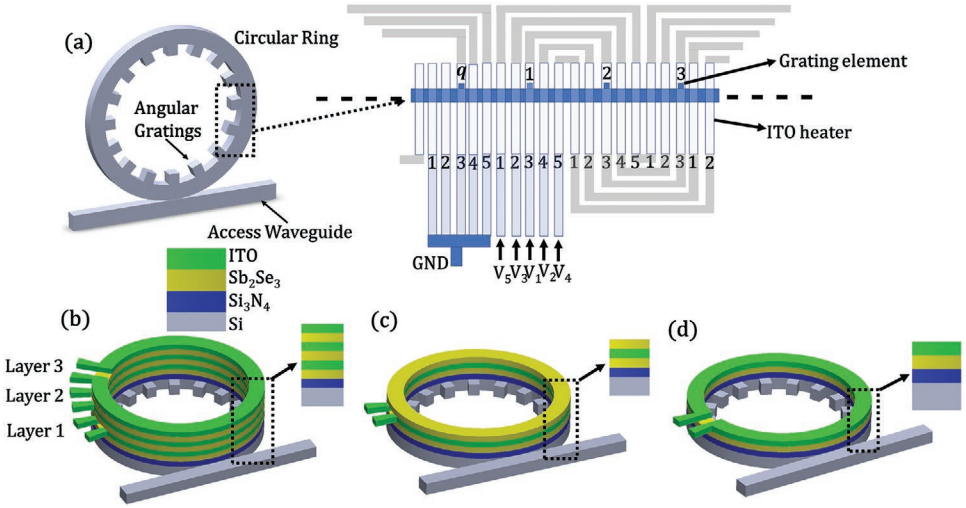

Figure 4. Schematic of ITO micro/nano heater-based OAM generator: a) design 1, b) design 2, c) design 3, and d) design 4.

case, three different layers of ITO rings are placed on top of three different Sb_2Se_3 rings of the same radius as the Si ring instead of five segmented ITO nano-heaters. Similar to design 1, the Si ring resonator with azimuthal grating elements and an access waveguide is buried within a very thin (50 nm) Si_3N_4 layer. Then, three successive thin Sb_2Se_3 ring layers and ITO ring layers are placed on top of the Si ring resonator. Layers 1 (L_1), 2 (L_2), and 3 (L_3) of ITO rings are connected to three different ultra-short pulse voltage sources V_1, V_2, and V_3, respectively. The layer closest to the Si ring resonator (L_1) has more impact while L_3 has the lowest impact in affecting the overall effective refractive index of the Si ring resonator by changing the phase of the PCM film. Initially, a high fraction of Sb_2Se_3 layers is considered to be in an amorphous state which can excite $l = -3$. Therefore, by applying different voltages at different layers other OAM modes can be excited according to **Table 1**. After achieving an $l = +2$ OAM mode, higher voltages with a shorter pulse are applied on all nano-heater layers (L_1, L_2, and L_3), and the appropriate fraction of the Sb_2Se_3 rings can be brought back to an amorphous state to achieve an $l = -3$ OAM mode.

This design has the flexibility to be used in direct electrical switching by applying voltage across the two different ITO layers. In this case, ITO layers act as electrodes only not as heaters and the heat generation is caused by the joule heating of Sb_2Se_3 film due to current flow through itself.[43]

Design 3: Figure 4c represents another tunable OAM generator consisting of bi-layer Sb_2Se_3 rings and only one ITO ring nano-heater sandwiched between them. This is a more simplified design compared to designs 1 and 2. Similar to designs 1 and 2, the Si-ring resonator and access waveguide are buried within a very thin Si_3N_4 layer, and two thin Sb_2Se_3 ring layers are separated by a thin ITO nano-heater ring placed on top of it. A tunable OAM wave can be generated by applying a pulse voltage of different magnitudes or pulse duration. In this case, only one nano-heater acts as a heat source and raises the temperature of both the Sb_2Se_3 rings simultaneously. The magnitude of the pulse voltage and the pulse duration can be experimentally determined to excite different OAM modes.

Design 4: Figure 4d represents the simplest design for a tunable OAM generator. In this design, only one Sb_2Se_3 ring and one ITO nano-heater are used. By applying varying pulse voltages of different magnitudes or pulse duration, several OAM modes can be tuned by changing the phase of the appropriate fraction of the Sb_2Se_3 film ring from amorphous to crystalline and vice versa. In order to achieve the same number of OAM modes as design 3, a comparatively thicker Sb_2Se_3 ring is required which needs to be reversibly switchable which can be challenging due to the poor thermal conductivity of the Sb_2Se_3 film.

The comparison of the designs is summarized as follows.

The main advantage of the first design is that it provides more controllability by applying five different voltage pulses at the same layer. However, this design has two main challenges:

1) Sb_2Se_3 film rings should be thicker to cover a specific number of OAM modes which need to be reversibly switchable through thermal heating.
2) The long, thin ITO nano-heaters passing through all grating elements are prone to break due to fabrication failure and overheating.

Table 1. Generation of different OAM modes by applying pulse voltages at different layers.

Pulse voltage V3	Pulse voltage V_2	Pulse voltage V_1	OAM mode (l)
-	-	-	−3
L_3		-	−2
	L_2		−1
L_3	L_2		0
	L_2	L_1	+1
L_3	L_2	L_1	+2
L_3 (higher voltage shorter pulse)	L_2 (higher voltage shorter pulse)	L_1 (higher voltage shorter pulse)	−3

The second design overcomes the drawbacks of the first design:

1) It requires comparatively thinner Sb_2Se_3 films to accommodate more OAM modes.
2) It uses three wider ITO rings as nano-heaters which are more robust and not prone to failure.

However, the main disadvantages of the second design are:

1) It requires multilayer fabrication steps.
2) Multiple ITO layers reduce the OAM wave intensity.
3) The third Sb_2Se_3 film layer has less effect on tuning OAM modes as it is comparatively far away from the Si-ring resonator.

The third design is a simplified version of design 2. Therefore, it has the same advantages as design 2 but overcomes the drawbacks:

1) It only requires three different layers (two Sb_2Se_3 layers and one ITO layer sandwiched in between) which reduce the fabrication complexity, and the OAM wave radiation intensity is less affected.
2) It requires only a single voltage source. In this design, different OAM modes can be achieved by tuning the magnitude and pulse width of the single voltage source. Although it uses fewer multilayers, it is a compromise between designs 1 and 2 with more tunability and a robust design with more outcomes.

The fourth design is the simplest and uses only a single layer of Sb_2Se_3 film and one ITO nano-heater. This design is easier to fabricate and tune to different OAM modes. However, the main challenge is that:

It requires a thicker Sb_2Se_3 film compared to design 3 for achieving the same number of OAM modes which is difficult to fully reamorphize as the amorphization requires the Sb_2Se_3 film to melt and cool down at a higher rate than the crystallization speed. Therefore, it has the challenge to tune more OAM modes by reversible switching of comparatively thicker Sb_2Se_3 film compared to other designs which use comparatively thinner Sb_2Se_3 films that are split.

5. Proposed Fabrication Technique

Initially, the access waveguide and the Si ring resonator can be fabricated with regular E-beam lithography or stepper-scanner process. Next, 50 nm thin LPCVD Si_3N_4 layer can be deposited on top followed by 105 nm/85 nm Sb_2Se_3 film and 120 nm/85 nm ITO film.[44] For bilayer Sb_2Se_3 design another layer of Sb_2Se_3 will be deposited. Finally, 50 nm low temperature PECVD Si_3N_4 will be coated on top of it (grown at sub 200 C temperatures to avoid damaging the PCM layer). After the deposition, the sample can be spin coated with maN-2403 electron beam resist (negative resist). Then the sample will be aligned in the high-resolution E-beam chamber to expose the ring area only. After the e-beam exposer, the sample can be developed by MFTM-319. Finally, the sample will be etched to remove Sb_2Se_3 and ITO except from the ring region.

6. Thermal Modeling of the Switching Behavior of the Sb_2Se_3 Film Using an ITO Nano-Heater

We have investigated the effectiveness of the simplest design (design 4) with only one Sb_2Se_3 ring and one ITO nano-heater ring using rigorous finite element calculations. We have considered a 220-nm-thick, 550-nm-wide Si access waveguide and ring resonator (**Figure 5**a). The device model is based on a standard SOI wafer. Therefore, the Si waveguide and the ring resonator are on top of the thermal oxide (SiO_2) and buried in 50-nm LPCVD Si_3N_4 layer. A 105-nm-thick Sb_2Se_3 ring, followed by a 120-nm-thick ITO nano-heater open ring with extended electrodes, is considered to be on top of the Si-ring resonator. The width of the Sb_2Se_3 ring and ITO nano-heater are considered 600 nm (slightly larger than that of the Si-ring resonator). The Sb_2Se_3 and ITO rings are covered by 1.5-µm-thick Si_3N_4 that could be grown via PECVD at a temperature lower than the melting temperature of Sb_2Se_3 (≈610 °C). We performed FEM simulations in COMSOL Multiphysics software to find the relation between the amplitude and pulse duration of the applied pulse voltage with the phase change of the fractional volume

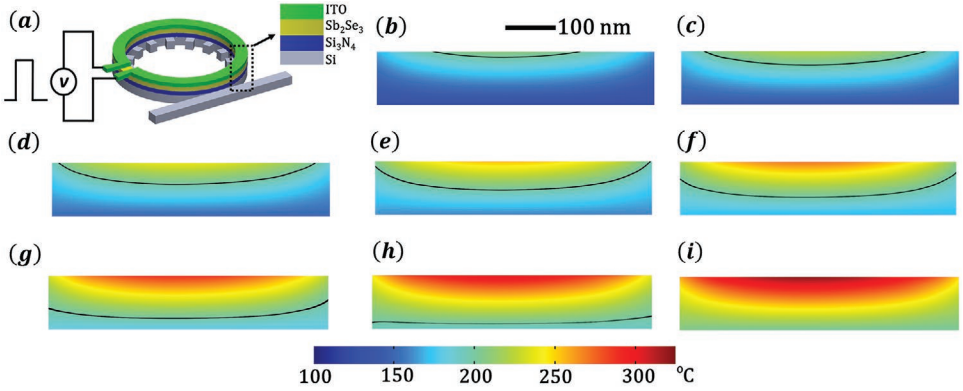

Figure 5. Temperature distribution in 105 nm Sb_2Se_3 film of tunable OAM generator while applying 1 µs pulse voltage of different amplitude across the ITO nano-heater. a) Schematic of the tunable OAM generator using single layer Sb_2Se_3 film and ITO film nano-heater ring. b–i) Temperature distribution along the cross-section of the Sb_2Se_3 film, the horizontal color bars represent the temperature in °C, the black contour line represents the boundary of 200 °C inside the Sb_2Se_3 film. b) 13.0 volts, c) 13.5 volts, d) 14.0 volts, e) 14.5 volts, f) 15.0 volts, g) 15.5 volts, h) 16 volts, and i) 16.5 volts.

of the Sb_2Se_3 layer from amorphous to crystalline state. The material properties of Sb_2Se_3, ITO, Si_3N_4, and Si used in this simulation are taken from published literature.[45–51] Figure 5 represents the cross-sectional view of the temperature distribution in Sb_2Se_3 film at 1 µs when 1 µs pulse voltages of different magnitude are applied. From Figure 5b–i it is observed that by changing the magnitude of the pulse voltage from 13 volts to 16.5 volts, the 105 nm Sb_2Se_3 can be transformed from partially to fully crystalized. As shown in Figure 5, around 3.5% of the volume fraction of the Sb_2Se_3 ring film exceeds the crystallization temperature of 200 °C for a 13-volt 1 µs pulse. Around 15%, 30%, 45%, 60%, 80%, 90%, and 100% of the Sb_2Se_3 film reach 200 °C or above when 13.5, 14, 14.5, 15, 15.5, 16 and 16.5 volts of 1 µs pulses are respectively applied. Therefore, different volume fractions of the Sb_2Se_3 layer can be crystallized by applying 1 µs pulses of different magnitudes. This change of phase of Sb_2Se_3 introduces the change of effective refractive index of the Si-ring resonator with azimuthal grating elements, and different OAM modes can be generated while the access waveguide is excited with TE_{01} mode of same wavelength. However, the most challenging aspect of this process is to reamorphize the crystallized Sb_2Se_3 layer because it requires the temperature to be raised above the melting point (610 °C) and to cool down faster than the crystallization kinetics. At the same time, the temperature of the ITO film must stay well below its melting point. The thermal conductivities of the PCM and the surrounding material are important for raising the temperature of most or all of the volume fraction of the PCM film above the melting point while keeping the temperature of the ITO well below its melting point.[51,52] The thermal conductivity of ITO[47,53] and silicon nitride[48] are more than two orders of magnitude higher than the thermal conductivity of Sb_2Se_3 (0.037 W mK^{-1}).[46]

Figure 6a–i shows a comparative study of the temperature distribution and cooling rate inside the two different thick (105 nm corresponding to design 4 and bi-layer 85 nm corresponding to design 3) Sb_2Se_3 film when comparatively higher voltages of shorter pulse are applied in ITO nano-heater to almost completely melt the Sb_2Se_3 and bring the film back to the amorphous state by rapid cooling. The blue solid lines in Figure 6a,d represent the maximum temperature of ITO film of around 1250 and 1480 °C for the proposed design (4 and 3) when 33 volts and 30 volts 650 ns pulse are applied across

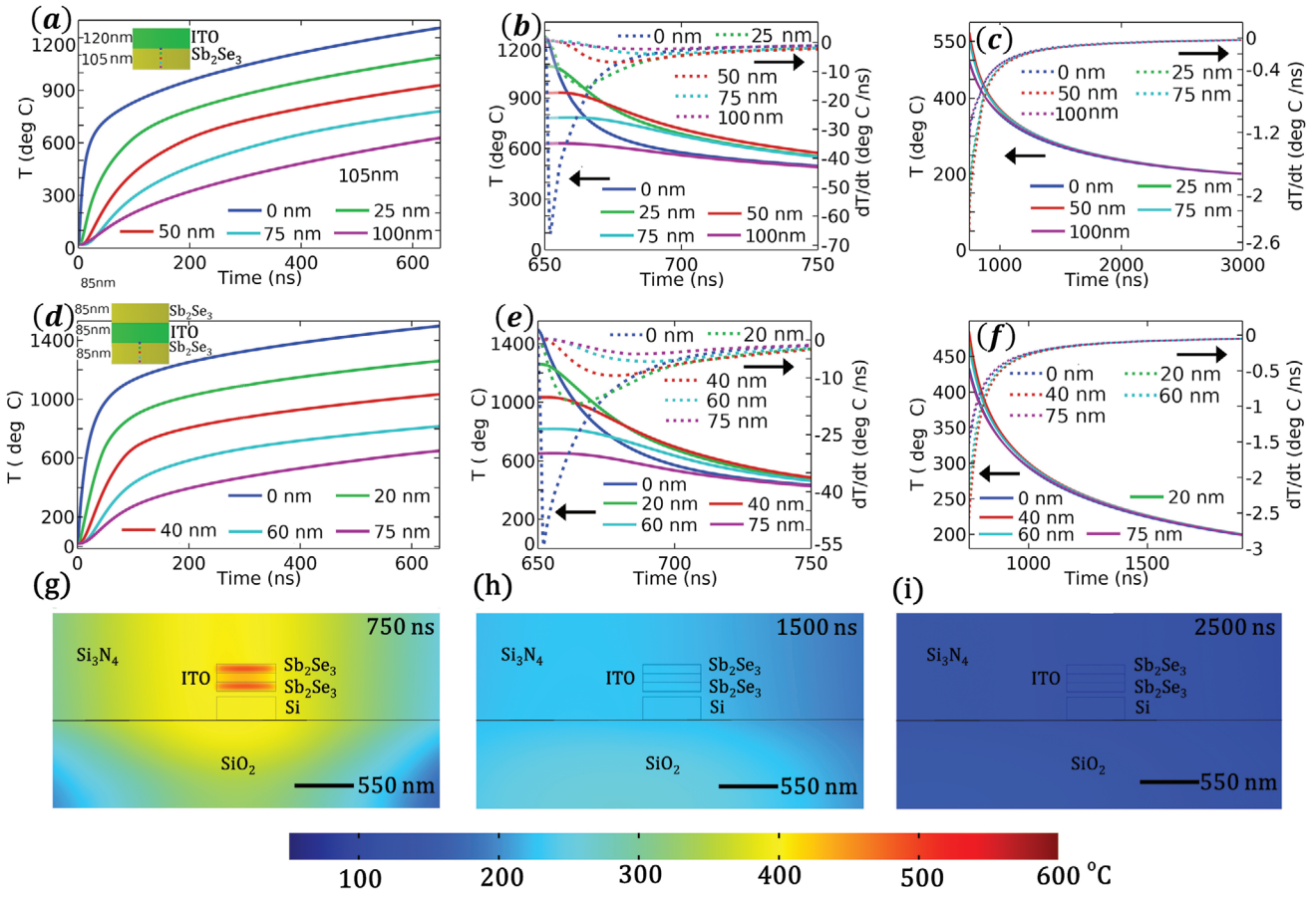

Figure 6. Temperature and cooling rate versus time at the center and along the depth of the ring (as shown in the inset of (a) and (d)) for applied 650 ns pulse voltage across the ITO ring of tunable OAM generators. The solid lines represent temperature in °C, dotted lines represent cooling rate. (a–c) corresponds to design 4: single layer 105 nm thick Sb_2Se_3 and 120 nm thick ITO ring; (d–f) correspond to design 3: bilayer 85 nm Sb_2Se_3 and sandwiched 85 nm thick ITO film ring). 33 and 30 volts are applied for design 4 and design 3, respectively. Blue lines (solid/dotted) represent the temperature and cooling rate of the ITO layer at the interface of ITO and Sb_2Se_3 film. The green, red, cyan, and purple (solid/dotted) lines in (a–c) represent the temperature and cooling rate of Sb_2Se_3 film at 25, 50, 75, and 100 nm depth from the ITO and Sb_2Se_3 film layers' interface, respectively. But, for (d,e) the green, red, cyan, and purple (solid/dotted) lines correspond to that of 20, 40, 60, and 75 nm depth. g–i) Heat dissipation in bi-layer Sb_2Se_3 film and surrounding region. Temperature distribution at g) 750 ns (after 100 ns of the pulse turned off), h) 1500 ns, and i) 2500 ns.

the ITO ring respectively. In this case, the Sb_2Se_3 film up to around 100 nm depth out of 105 nm depth is completely melted (>610 °C) at 650 ns (Figure 6a), and similarly up to around 75 nm depth out of 85 nm depth is melted (Figure 6d) as shown by the purple lines. Figure 6b,e represents temperature and cooling rate for the first 100 ns after the applied pulse voltage is switched off (from 650 ns to 750 ns). It is observed that within less than the 100 ns both the films (design 4: 105 nm Sb_2Se_3 and design 3: bi-layer 85 nm Sb_2Se_3) cool down to solid (<610 °C). The cooling rate of a film depends upon the temperature and thermal conductivity of the film and the surrounding materials. The cooling rate of ITO is initially much higher than that of Sb_2Se_3 as shown by the dotted blue lines and the thicker 120 nm ITO (Figure 6b) cools faster than the thinner 85 nm ITO (Figure 6e). However, the thinner Sb_2Se_3 cools faster than that of the thicker Sb_2Se_3 as observed comparing the red, green, cyan and purple dotted lines in Figure 6b,e. From Figure 6c,f, it is observed the 85 nm Sb_2Se_3 film (of proposed design 3) completely goes blow the crystallization temperature (200 °C) within 1900 ns while it takes up to around 3000 ns for the 105 nm film (design 4) to reach below the crystallization temperature. Therefore, although it is possible to crystallize a thicker layer of Sb_2Se_3 film, it may not be possible to reamorphize most of the comparatively thicker Sb_2Se_3 film. Therefore, considering the crystallization and re-amorphization of a larger fraction of the Sb_2Se_3 film while maintaining tunability of more OAM modes, it is preferable to use design 3 which has two split 85-nm Sb_2Se_3 layers with an 85 nm ITO nano-heater sandwiched between them compared to design 3 of thicker film. Figure 6g–i represents the temperature distribution in bi-layer PCM film and the surrounding region. After the generation of high heat by the applied electric pulse both the ITO and the PCM cool down within a few microseconds due to the presence of a comparatively larger volume of higher thermally conductive material (Si_3N_4 and ITO). From Figure 6g it is observed that at 750 ns of applied 650 ns pulse the temperature of most of the surrounding region reaches below 500 °C except inside the PCM layer. The temperature of the surrounding region goes below 300 and 200 °C within 1.5 and 2.5 µs respectively. It is to be noted that the refractive index of the PCM which depends on the crystallization fraction based on the temperature distribution and the cooling rate of the thermal excitation process should be stable to achieve a stable OAM wave. However, there is a transition moment to switch from one OAM mode to another OAM mode. At this transition moment, the PCM will be heated and then cooled down to a steady state level to change its phase to a stable level. While transitioning, the ring resonator will be off resonance but at the steady level, the ring resonator will be at a resonance provided that the overall effective refractive index of the ring resonator satisfies the resonance condition due to phase change of the PCM. This implies that through the transition, there will be little output from the resonator as there is not sufficient buildup of intensity due to off resonance, until the required partial or full switching happens and we are "locked" into resonance. At this point, the ring resonator will continue to provide a stable OAM wave until the PCM is heated again to switch to another OAM state.

Figure 7 demonstrates the generation of several different OAM modes with their corresponding efficiencies for the proposed Si ring resonator with 85 nm bi-layer Sb_2Se_3 and 85 nm ITO film ring in between them (design 3). The effect of device parameters, presence or absence of grating elements at different ring layers on OAM generation efficiency, the effect of increase of partial crystallization on propagation mode profile, and the effect of presence of lossy ITO on the OAM pattern distortion and radiation efficiency have been analyzed. For 120 nm coupling gap and 81.7 nm grating length/width OAM wave of $l_{TC} = -3$, $l_{TC} = -2$, $l_{TC} = -1$, $l_{TC} = 0$, $l_{TC} = +1$, $l_{TC} = +2$, $l_{TC} = +3$ are observed at partial crystallization correspond to the overall PCM refractive index of 3.3475, 3.48, 3.61, 3.7175, 3.81, 3.89, and 3.96 respectively with efficiency of 2.18%, 1.45%, 0.78%, 0.55%, 0.33%, 0.26%, and 0.14% respectively as shown in Figure 7a. Figure 7b represents the corresponding phase of the generated OAM wave. The efficiency of the generated wave can be increased to 4.53%, 3.22%, 1.92%, 1.40%, 0.70%, 0.43%, and 0.20% by decreasing the coupling gap to 60 nm and increasing the grating length to 100 nm similar to that observed for 105 nm single layer Sb_2Se3. The efficiency can be further significantly increased to 7.15%, 5.56%,3.68%, 3.34%, 1.72%, 1.3%, and 0.77% by applying grating elements on all the ring layers as shown in Figure 7c,f. Figure 7f shows the comparison of the corresponding radiation efficiency. It is to be noted that compared to the 105 nm single layer Sb_2Se3 film the radiation efficiency of 85 nm bi-layer Sb_2Se_3 is lower which is attributed to the proximity of the lossy ITO layer. For this design 3, the ITO film is closer to the Si ring resonator (135 nm) compared to that of design 4 (155 nm). Figure 7c,d represents the intensity of the generated OAM wave and mode profile for multilayer grating element with 60 nm coupling and 100 nm grating extrusion length. From Figure 7d, it is observed that more light is confined into the PCM layers with the increase of the partial crystallization of PCM which also causes lower radiation efficiency. Moreover, due to the presence of 85 nm lossy ITO layer film in between the PCM layers the intensity of the electric field decreases while light traversing around the ring as shown in Figure 7e. From Figure 7e, it is observed that the intensity of the light in the ring at the right-bottom side is more compared to the other part of the ring. This non-uniform angular intensity pattern causes non-uniform radiation from each grating element, therefore, the OAM angular intensity pattern becomes non-uniform as shown in Figure 7a,c. However, a uniform electric field intensity distribution is observed inside the ring resonator when the imaginary part of the ITO refractive index is considered to be zero. As a result, a uniform intensity distribution is observed in the field pattern of the OAM wave. The corresponding radiation efficiency is found to be 25.5% which is very high and similar to that of the OAM generator without any PCM/ITO layers. This simulation result implies that the complex refractive index of the ITO is responsible for the lower efficiency and deformation of the OAM pattern (Figure 7f). Therefore, it is very important to use an optimized ITO film fabrication process which results in a very low value of extinction coefficient.

7. Conclusion

In this work, an integrated photonic device for the generation of rapidly tunable OAM waves at 1550 nm using an ultra-low-loss

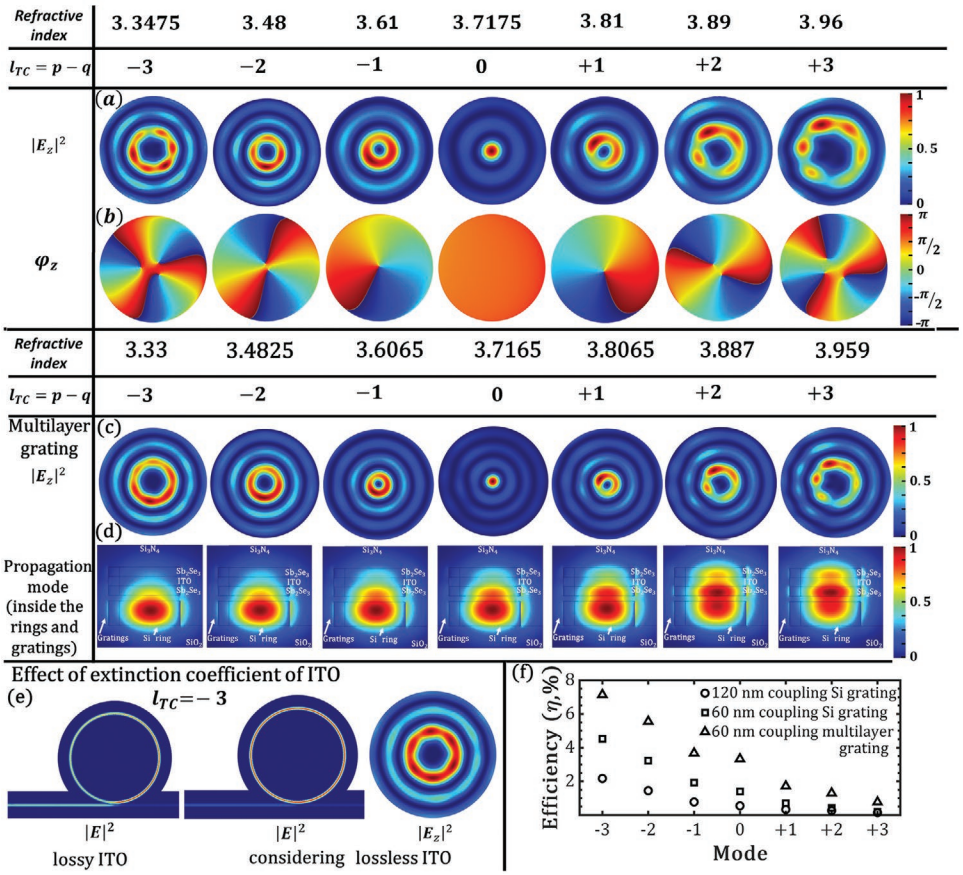

Figure 7. Generation of different OAM wave modes at 1550 nm by embedding bilayer 85 nm Sb_2Se_3 film rings with an ITO nano-heater between them. a) Longitudinal component of generated CVVs ($|E_z|^2$) showing topological charge of OAM waves $l = -3, -2, -1, 0, +1, +2, +3$ at 1550 nm wavelength by considering overall refractive index of Sb_2Se_3 as 3.3475, 3.48,3.61, 3.7175,3.81,3.89, and 3.96 respectively as an effect of partial phase change, coupling gap = 120 nm, width/length of grating element = 81.7 nm, grating elements on Si ring resonator only, b) Corresponding spiral phase pattern for $l = -3, -2, -1, 0, +1, +2, +3$, c) Longitudinal component of electric field intensity ($|E_z|^2$) of different OAM modes $l = -3, -2, -1, 0, +1, +2, +3$ for coupling gap = 60 nm, width of grating element = 81.7 nm, extrusion length of grating element = 100 nm, multilayer (Si, PCM, ITO) grating elements. d) Mode profile inside the ring resonator with 60 nm coupling gap, multilayer grating. The electric field tends to leak from the Si ring and confines more in the PCM ring layer with the increase of the crystallization phase. e) Electric field intensity inside the ring resonator for lossy ITO and considering lossless (imaginary part of the refractive index = 0) ITO (coupling gap = 60 nm, and multilayer grating elements), and ($|E_z|^2$) of the generated OAM wave considering lossless ITO. f) Efficiency of the radiated OAM wave of different modes $l = -3, -2, -1, 0, +1, +2, +3$: Circles correspond to coupling gap of 120 nm, grating width/length = 81.7 nm, Si ring grating only; squares correspond to coupling gap of 60 nm, grating width = 81.7 nm, grating extrusion length = 100 nm, Si grating only; and triangles correspond to coupling gap of 60 nm, grating width = 81.7 nm, grating extrusion length = 100 nm, grating elements are present at all (Si, PCM and ITO ring) layers.

PCM (Sb_2Se_3) and an ITO film-based nano-heater has been demonstrated through rigorous numerical modeling. Different design options and their corresponding advantages and drawbacks are described in detail. FEM analysis is conducted on a silicon ring resonator with grating elements to observe different OAM modes at different wavelengths in the telecom band and an ultra-low loss PCM (Sb_2Se_3) film with ITO nano-heater is introduced to achieve tunable OAM emission. Initially, a simple design is revealed using a Sb_2Se_3 film as a tuning layer by considering the average change of refractive index of the film due to different volume fractions of the crystallized phase to tune various OAM modes at 1550 nm. Next, a critical analysis of different realistically implementable design options with an ITO nano-heater and short pulse voltage to fractionally change the phase of the Sb_2Se_3 film is presented. FEM analysis is conducted to demonstrate the inherent phase change dynamics within the tuning film by analyzing the temperature distribution and cooling rate of Sb_2Se_3 film which allows us to check the potential tunability of the proposed device. A comparative study of ITO nano-heater based reversible phase change of a single layer 105 nm Sb_2Se_3 with 120 nm ITO ring and a bilayer 85 nm Sb_2Se_3 with 85 nm ITO ring on a silicon ring resonator is conducted. According to the thermal analysis, the bilayer thinner Sb_2Se_3 film is found to be more suitable than the thicker single layer Sb_2Se_3 to achieve more OAM modes due to its higher cooling rate providing more possibility of reversible switching of the large volume fraction of the PCM film. Finally, the OAM generation of $l = -3, -2, -1, 0, +1, +2, +3$ is verified using thinner 85 nm bi-layer Sb_2Se_3 film. However, the corresponding efficiency of the bi-layer Sb_2Se_3 film is found to be lower compared to the single-layer 105 nm PCM layer which is attributed to the proximity of the lossy ITO layer. An important

conclusion from our work is that there is a compromise between the number of achieved OAM modes and the radiation efficiency of the different design options. This proposed design will guide researchers toward implementing ultra-fast, tunable OAM generation or tunable OAM transceivers using on-chip integrated Si photonic devices.

Acknowledgements

J.R.H. acknowledges support from the Air Force Office of Scientific Research (Program Manager Dr. Gernot Pomrenke) under award number FA9550-20RYCOR059. M.S.A. and I.A. acknowledge the funding through the Small Business Office under award number FA8650-18-P-1700 and the National Science Foundation under grant number ECCS-17100273.

Conflict of Interest

The authors declare no conflict of interest.

Data Availability Statement

The data that support the findings of this study are available from the corresponding author upon reasonable request.

Keywords

free-space optical communications, optical vortex beams, orbital angular momentum, phase change materials

Received: January 15, 2022
Revised: June 19, 2022
Published online: July 17, 2022

[1] A. M. Yao, M. J. Padgett, *Adv. Opt. Photonics* **2011**, *3*, 161.
[2] N. Bozinovic, Y. Yue, Y. Ren, M. Tur, P. Kristensen, H. Huang, A. E. Willner, S. Ramachandran, *Science* **2013**, *340*, 1545.
[3] J. Wang, J.-Y. Yang, I. M. Fazal, N. Ahmed, Y. Yan, H. Huang, Y. Ren, Y. Yue, S. Dolinar, M. Tur, A. E. Willner, *Nat. Photonics* **2012**, *6*, 488.
[4] J. Leach, B. Jack, J. Romero, A. K. Jha, A. M. Yao, S. Franke-Arnold, D. G. Ireland, R. W. Boyd, S. M. Barnett, M. J. Padgett, *Science* **2010**, *329*, 662.
[5] M. Padgett, R. Bowman, *Nat. Photonics* **2011**, *5*, 343.
[6] T. F. Scott, B. A. Kowalski, A. C. Sullivan, C. N. Bowman, R. R. McLeod, *Science* **2009**, *324*, 913.
[7] X. Cai, J. Wang, M. J. Strain, B. Johnson-Morris, J. Zhu, M. Sorel, J. L. O'Brien, M. G. Thompson, S. Yu, *Science* **2012**, *338*, 363.
[8] L. Allen, M. W. Beijersbergen, R. J. C. Spreeuw, J. P. Woerdman, *Phys. Rev. A* **1992**, *45*, 8185.
[9] M. N. Malik, N. Zhang, V. Toccafondo, C. Klitis, M. Lavery, A. Sgambelluri, J. Zhu, X. Cai, S. Yu, G. Preve, M. Sorel, A. Bogoni, M. Scaffardi, *J. Lightwave Technol.* **2021**, *39*, 91.
[10] Y. Guo, S. Zhang, M. Pu, Q. He, J. Jin, M. Xu, Y. Zhang, P. Gao, X. Luo, *Light: Sci. Appl.* **2021**, *10*, 63.
[11] Y. Shen, X. Wang, Z. Xie, C. Min, X. Fu, Q. Liu, M. Gong, X. Yuan, *Light: Sci. Appl.* **2019**, *8*, 90.
[12] T. Lei, M. Zhang, Y. Li, P. Jia, G. N. Liu, X. Xu, Z. Li, C. Min, J. Lin, C. Yu, H. Niu, X. Yuan, *Light: Sci. Appl.* **2015**, *4*, e257.
[13] C. de Lisio, E. Karimi, E. Santamato, F. Cardano, L. Marrucci, S. Slussarenko, *Appl. Opt.* **2012**, *51*, C1.
[14] D. Park, F. K. Fatemi, M. Bashkansky, *Opt. Express* **2010**, *18*, 212.
[15] B. C. Lim, H. H. Teo, K. S. Tiaw, M. H. Hong, P. B. Phua, W. J. Lai, *Opt. Express* **2008**, *16*, 15694.
[16] M. Pu, X. Li, X. Ma, Y. Wang, Z. Zhao, C. Wang, C. Hu, P. Gao, C. Huang, H. Ren, X. Li, F. Qin, J. Yang, M. Gu, M. Hong, X. Luo, *Sci. Adv.* **2015**, *1*, e1500396.
[17] G. Milione, S. Evans, D. A. Nolan, R. R. Alfano, *Phys. Rev. Lett.* **2012**, *108*, 190401.
[18] M. Zahidy, Y. Liu, D. Cozzolino, Y. Ding, T. Morioka, L. K. Oxenløwe, D. Bacco, *Nanophotonics* **2022**, *11*, 821.
[19] L. Meriggi, M. Sorel, Q. Xiao, S. Li, S. Yu, W. Yu, X. Cai, Z. Nong, *Opt. Lett.* **2017**, *42*, 975.
[20] S. Mochizuki, X. Gu, K. Tanabe, A. Matsutani, M. Ahmed, A. Bakry, F. Koyama, *Appl. Phys. Express* **2014**, *7*, 022502.
[21] G. Rui, Q. Zhan, R. L. Nelson, *Opt. Express* **2012**, *20*, 18819.
[22] Z. Xie, T. Lei, F. Li, H. Qiu, Z. Zhang, H. Wang, C. Min, L. Du, Z. Li, X. Yuan, *Light: Sci. Appl.* **2018**, *7*, 18001.
[23] D. Coolbaugh, G. Leake, J. Sun, M. R. Watts, M. Moresco, *Opt. Lett.* **2014**, *39*, 5977.
[24] C. R. Doerr, N. K. Fontaine, M. Hirano, T. Sasaki, L. L. Buhl, P. J. Winzer, in *37th European Conference and Exposition on Optical Communications*, Optica Publishing Group, Washington DC **2011**, p. Th.13.A.3.
[25] J. Sun, A. Yaacobi, M. Moresco, D. Coolbaugh, M. R. Watts, in *CLEO: 2015 Postdeadline Paper Digest*, Optica Publishing Group, Washington DC **2015**, p. JTh5A.5.
[26] M. Delaney, I. Zeimpekis, D. Lawson, D. W. Hewak, O. L. Muskens, *Adv. Funct. Mater.* **2020**, *30*, 2002447.
[27] P. Pintus, M. Hofbauer, C. L. Manganelli, M. Fournier, S. Gundavarapu, O. Lemonnier, F. Gambini, L. Adelmini, C. Meinhart, C. Kopp, F. Testa, H. Zimmermann, C. J. Oton, *Laser Photonics Rev.* **2019**, *13*, 1800275.
[28] E. G. Johnson, G. White, J. K. Miller, K. S. Morgan, R. J. Watkins, W. Li, Y. Li, *Opt. Express* **2019**, *27*, 3920.
[29] N. Zhang, M. Scaffardi, C. Klitis, M. N. Malik, V. Toccafondo, F. Fresi, J. Zhu, X. Cai, S. Yu, A. Bogoni, M. Sorel, *arXiv: 2008.00680* **2020**.
[30] J. Zhu, S. Yu, X. Cai, Y. Zhang, Y. Chen, *Opt. Lett.* **2014**, *39*, 4435.
[31] J. Zhu, S. Yu, X. Cai, Y. Chen, *Opt. Lett.* **2013**, *38*, 1343.
[32] G. Rui, B. Gu, Y. Cui, Q. Zhan, *Sci. Rep.* **2016**, *6*, 28262.
[33] Q. Zhan, *Opt. Lett.* **2006**, *31*, 867.
[34] Z. Shao, J. Zhu, Y. Chen, Y. Zhang, S. Yu, *Nat. Commun.* **2018**, *9*, 926.
[35] Y. Zhang, C. Fowler, J. Liang, B. Azhar, M. Y. Shalaginov, S. Deckoff-Jones, S. An, J. B. Chou, C. M. Roberts, V. Liberman, M. Kang, C. Ríos, K. A. Richardson, C. Rivero-Baleine, T. Gu, H. Zhang, J. Hu, *Nat. Nanotechnol.* **2021**, *16*, 661.
[36] Z. Fang, J. Zheng, A. Saxena, J. Whitehead, Y. Chen, A. Majumdar, *Adv. Opt. Mater.* **2021**, *9*, 2002049.
[37] M. Delaney, I. Zeimpekis, H. Du, X. Yan, M. Banakar, D. J. Thomson, D. W. Hewak, O. L. Muskens, *Sci. Adv.* **2021**, *7*, 3500.
[38] Y. Zhang, C. Ríos, M. Y. Shalaginov, M. Li, A. Majumdar, T. Gu, J. Hu, *Appl. Phys. Lett.* **2021**, *118*, 210501.
[39] S. K. Bahl, K. L. Chopra, *J. Appl. Phys.* **1969**, *40*, 4940.
[40] Z. Ma, Z. Li, K. Liu, C. Ye, V. J. Sorger, *Nanophotonics* **2015**, *4*, 198.
[41] A. Yariv, *IEEE Photonics Technol. Lett.* **2002**, *14*, 483.
[42] D. L. P. Vitullo, S. Zaki, D. E. Jones, M. Sumetsky, M. Brodsky, M. Brodsky, *Opt. Express* **2020**, *28*, 25908.
[43] C. Liu, Y. Yuan, L. Cheng, J. Su, X. Zhang, X. Li, H. Zhang, M. Xu, J. Li, *Results Phys.* **2019**, *13*, 102228.
[44] J. A. Burrow, M. S. Alam, E. M. Smith, R. Yahiaoui, R. Laing, P. J. Shah, T. A. Searles, S. Vangala, J. R. Hendrickson, A. Sarangan, I. Agha, *arXiv: 2111.09940* **2021**.

[45] A. S. Pashinkin, A. S. Malkova, M. S. Mikhailova, *Russ. J. Phys. Chem. A* **2008**, *82*, 1035.
[46] T.-Y. Y. Ko, M. Shellaiah, K. W. Sun, *Sci. Rep.* **2016**, *6*, 35086.
[47] D. Thuau, I. Koymen, R. Cheung, *Microelectron. Eng.* **2011**, *88*, 2408.
[48] H. O. Pierson, *Handbook of Chemical Vapor Deposition: Principles, Technology and Applications*, William Andrew Publishing, Norwich, NY**1999**.
[49] H. R. Shanks, P. D. Maycock, P. H. Sidles, G. C. Danielson, *Phys. Rev.* **1963**, *130*, 1743.
[50] P. D. Desai, *J. Phys. Chem. Ref. Data* **2009**, *15*, 967.
[51] L. Wang, J. Wen, C. Yang, B. Xiong, *Sci. Technol. Adv. Mater.* **2018**, *19*, 791.
[52] O. J. Gregory, Q. Luo, E. E. Crisman, *Thin Solid Films* **2002**, *406*, 286.
[53] T. Ashida, A. Miyamura, N. Oka, Y. Sato, T. Yagi, N. Taketoshi, T. Baba, Y. Shigesato, *J. Appl. Phys.* **2009**, *105*, 073709.